Mechanical properties of molecularly thin lubricant layers: experimental methods and procedures

2005 J. Phys.: Condens. Matter 17 S319

(http://iopscience.iop.org/0953-8984/17/9/004)

INSTITUTE OF PHYSICS PUBLISHING JOURNAL OF PHYSICS: CONDENSED MATTER

J. Phys.: Condens. Matter **17** (2005) S319–S332 doi:10.1088/0953-8984/17/9/004

Mechanical properties of molecularly thin lubricant layers: experimental methods and procedures

Thomas Becker and Frieder Mugele

Department of Applied Physics, University of Ulm, Albert Einstein Allee 11, D-89069 Ulm, Germany

Received 24 November 2004
Published 18 February 2005
Online at stacks.iop.org/JPhysCM/17/S319

Abstract

We present a new experimental set-up and experimental strategies designed for investigating dynamic processes in molecularly thin lubricant layers. The experimental set-up is an extension of a conventional surface forces apparatus, which allows for two-dimensional imaging of the thickness of liquid layers confined between two atomically smooth mica surfaces. We present details of a mica surface preparation technique that eliminates otherwise frequently encountered contamination of the surfaces with nanoparticles, which were recently shown to affect surface forces measurements. Multiple-beam interferometry results in a thickness resolution of approximately 0.2 nm. The data analysis relies on fitting of numerically calculated optical transmission spectra of asymmetric multilayer Fabry–Perot interferometers. The lateral resolution and time resolution are determined by the optical resolution of the video microscopy and the frame rate of the digital CCD camera, respectively. Furthermore, we summarize several results and new insights into the collapse dynamics of thin lubricant layers that were obtained with this technique.

1. Introduction

Thin liquid films confined between solid substrates are ubiquitous both in Nature and in technology [1]. They play an important role in geological processes where water or oil penetrate porous rock material. Ultrathin capillaries help plants to raise water; membrane pores of molecular dimension allow for the exchange of water, ions, and other molecules between the interior of biological cells and their environment. Thin liquid lubricant layers reduce friction and wear in our hip and knee joints and carry the load of our bodies. Similarly, lubricant layers reduce friction and wear in bearings of any kind of machinery. Due to the ongoing miniaturization of mechanical devices, technologically relevant lubricant layers are becoming thinner and thinner, and will eventually approach molecular dimensions, as for instance in computer hard drives. The question of how confinement, molecular architecture, and the specific liquid–substrate interaction affect the structure and the mechanical properties

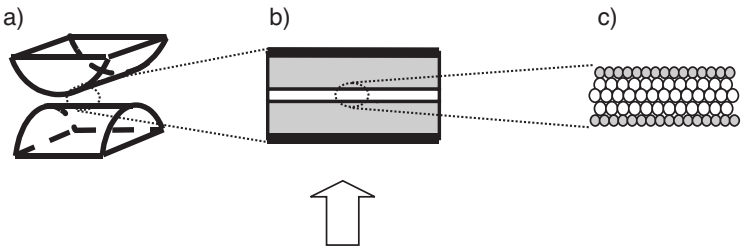

Figure 1. Sample geometry in a surface forces apparatus on different length scales. (a) Crossed cylinder geometry (typical radius of curvature of 2 cm). (b) Parallel plate geometry with Ag mirrors (thick solid lines), mica sheets (grey), and the liquid film (thin white rectangle). The arrow indicates the direction of the light used for the interferometric thickness measurement. (c) Layered structure of a molecularly thin film (grey: mica substrate atoms; white: liquid molecules).

of thin liquid films has become a focus of research in the area of nanotribology. While many practical aspects of lubrication depend strongly on the actual microscopic geometry and chemical composition of the solid surfaces, most fundamental progress was achieved in studies of well-defined model systems with controlled surfaces. The most important geometry is a model slit pore consisting of two atomically smooth single-crystalline surfaces at a separation of a few molecular diameters. Experimentally, this geometry is realized in the surface forces apparatus [2]. In this instrument, two mica sheets free of atomic steps over distances of hundreds of micrometres are mounted onto cylindrically curved sample holders and brought into contact at a well-defined position (figure 1(a)). At the apices, the two surfaces form a slit pore with parallel walls (figure 1(b)). Measurements of the force required to press the two surfaces together revealed that the molecules in simple liquids adopt a layer structure parallel to the surfaces (e.g. [3–8]) (see figure 1(c)). Under these conditions, the film thickness assumes only values corresponding to an integral multiple of the molecular diameter. Whenever the normal force exceeds a certain threshold value, one layer of molecules is squeezed out of the contact area and the film thickness is reduced correspondingly. In order to probe the mechanical properties of the liquid films, the two solid surfaces were sheared with respect to each other and the shear forces transmitted by the film were measured [4, 6–8]. Most of these measurements found that the viscosity increases with decreasing film thickness.

In the present paper, we describe the experimental set-up and the procedures developed for investigating the stability and the dynamics of squeeze-out of individual molecular layers. Instead of measuring forces, this technique relies on the direct optical imaging of the squeeze-out process using multiple-beam interferometry in conjunction with video microscopy. In section 2, we describe the mechanical and the optical part of the experimental set-up. Section 3 is devoted to specific experimental procedures including surface preparation and characterization as well as the data acquisition procedure and the numerical analysis of the multiple-beam interferometry data. Finally, in section 4, we present the two-dimensional imaging technique and give an overview of the most important results obtained with this method.

2. The experimental set-up

Figure 2 shows a schematic diagram of the overall set-up. The main elements are a xenon arc lamp (300 W; Mueller GmbH Elektronik-Optik, Germany), a grating monochromator, the SFA chamber inside a temperature-controlled box, and a CCD camera (PixelFly Standard HiRes 220XS; PCO Computer Optics GmbH, Germany). All of the components are mounted on an

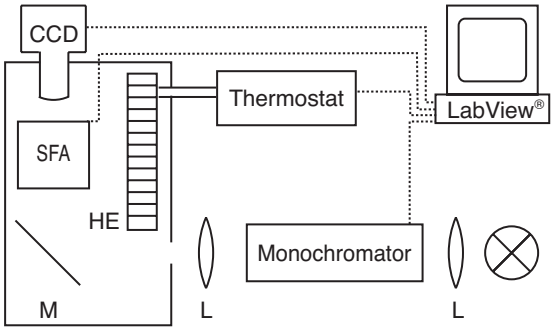

Figure 2. A schematic diagram of the experimental set-up (M: mirror; L: lenses; HE: heat exchanger).

optical table, except for the Xe arc lamp and its power supply, which rest on an independent table, in order to reduce vibrations. All major components are computer controlled via custom written LabView programs. We now describe the mechanical and the optical parts of the set-up.

2.1. The mechanical set-up

2.1.1. The sample chamber. We developed two sample chambers shown in figures 3(a) and (b), optimized for different applications. Set-up A (figure 3(a)) is a conventional surface forces apparatus. Set-up B (figure 3(b)) was specifically designed for performing simultaneously x-ray scattering experiments and optical multiple-beam interferometry with liquid films in a well-controlled confinement geometry. This latter set-up is mechanically extremely stable; however, it does not allow one to measure surface forces.

We first describe set-up A. The chamber is manufactured from stainless steel with a wall thickness of 10 mm. Both top and bottom plates are equipped with glass windows (thickness: 150 μm), which allow optical measurements in transmission. The top surface is attached to the top of the chamber via a leaf spring (typical spring constant: 100–200 N m^{-1}). The bottom surface is mounted on a stainless steel plate, which can be aligned and translated in three dimensions with five micrometre screws. Two of them are used for translation in the horizontal plane, in order to allow choice of different contact spots on the sample surfaces. The other three allow for parallel alignment of the two surfaces and for a coarse approach. Fine control of the liquid film thickness is achieved using magnetic forces [9]. To this end, the holder of the upper surface is equipped with one to four small NdFeB permanent magnets. Outside the SFA chamber, there is a magnetic coil which generates an inhomogeneous magnetic field at the sample position. The current through the coil is provided by a computer-controlled power supply (E3648A, Agilent Technologies). Depending on the number and strength of the magnets, the magnetic force on the sample holder is 10–30 mN A^{-1}. The maximum current through the coils is limited to 2.5 A in order to avoid excessive heat generation. The minimum current step is 1 mA, corresponding to a minimum force increment of 10–30 μN. Smaller forces can be generated by introducing spacers between the sample chamber and the coil or by exchanging the coil[1].

[1] Note that the force is generated on the flexible end of the leaf spring. Therefore, the spring bends when the surfaces are brought together by increasing the magnetic force. However, the spring does not deform any longer once the surfaces are in contact. This avoids the rolling motion in conventional SFA set-ups, where the springs bend upon increasing the load once the surfaces are in contact. This rolling motion produces undesired shear forces, which are usually avoided using a double-spring construction. Since the magnetic force generation does not produce rolling, a single-spring design is sufficient in our set-up.

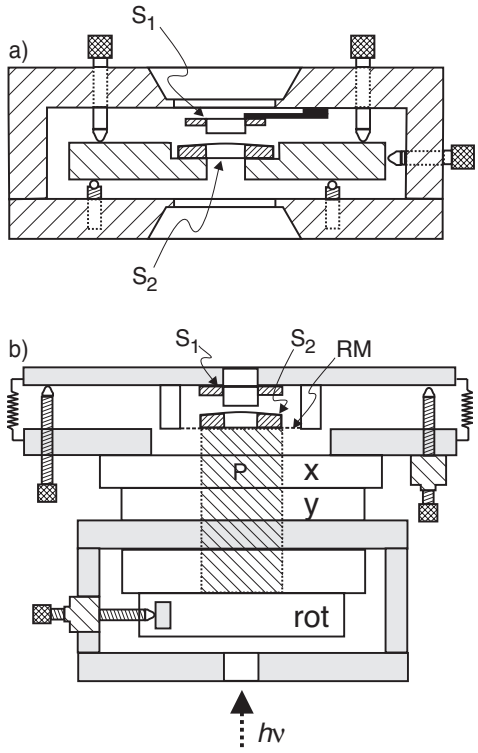

Figure 3. Sketches of the SFA set-ups. (a) Set-up A. Chamber diameter: 12 cm; S_1, S_2: top and bottom sample holders. (b) Set-up B, suitable for simultaneous x-ray scattering experiments. (P: piezo-tube; RM: rubber membrane; X, Y: transverse manual translation stages; rot: rotation stage; S_1, S_2: top and bottom sample holders). The dashed arrow indicates the direction of both optical and x-ray beams.

Set-up B (figure 3(b)) is characterized by a much smaller volume of the actual sample cell. In this set-up, the bottom surface is mounted on a piezo-tube (length: 2.5″; OD 0.5″, Staveley Sensors), which allows fine positioning. The outer electrode is split into four 90° segments such that shear forces can be applied to the sample by bending the piezo-tube. A HV amplifier with five independent channels (Elba Tech) and a DAAD board (16 bit resolution) allow for computer-controlled vertical displacement of ± 1.5 μm and a horizontal (shear) displacement of ± 8 μm. In addition, the piezo-tube is mounted on a rotation stage such that it can be rotated along its axis within a range of $\pm 5°$. The limits arise from the mechanical properties of a rubber membrane, which seals the gap between the top of the piezo-tube and the walls of the actual sample chamber (see figure 3(b)). The top surface is attached rigidly to the top plate of the sample cell. Three fine screws allow alignment and a coarse approach of the top plate. One of them is motorized with a piezo-motor (Picomotor 8322, New Focus) and can be controlled from the computer. The step width of the motor can be adjusted such that approach steps of the surfaces are of the order of 5 nm. The sample chamber (including the top surface) is mounted on a manual x–y translation stage. It can be translated by ± 3 mm relative to the piezo-tube and the bottom surface in order to change the location of the contact area on the surfaces.

Both set-ups can accommodate two different kinds of mica sample holders. Mica surfaces can either be glued to cylindrical lenses with a diameter of 1 cm (radius of curvature: 2 cm), as commonly used in surface forces experiments, or they can be glued onto thin (≈ 80 μm)

microscope cover slips. This second type of sample is then clamped onto curved stainless steel holders with holes in the centre that allow the passage of light. Currently, mounts with radii of curvature of 5, 7, and 10 cm are available. One advantage of these mounts is that the mica surfaces can be prepared in a flat configuration. While they are flat, the surfaces are easily amenable to additional characterization (e.g. AFM) or preparation steps (e.g. chemical patterning via microcontact printing). Only after the final preparation step are they clamped onto the curved holders.

Both sample chambers include a container for drying agent (typically phosphorus pentoxide (P_2O_5)).

2.1.2. The temperature control box. Both set-ups can be mounted inside a thermally insulated box. It consists of 10 mm thick PVC plates, which are covered on the inside with 15 mm thick plates of Styrofoam. The inner dimensions of the box are approximately $0.2 \times 0.3 \times 0.2$ m^3. There is an entrance window for the monochromatic light in the bottom of the cell. On the top, the microscope objective that captures the transmitted light penetrates slightly into the box. The gap between the objective and the box is sealed with a rubber membrane. The box can be purged with dry air in order to prevent water condensation during experiments at low temperatures. Inside the box, there is a liquid–air heat exchanger (WT200010, Tiger Electronics) with a low noise fan. An external computer-controlled thermostat (LAUDA RE306 Ecoline; heating power: 2.25 kW, cooling power at 20 °C: 0.2 kW) provides a continuous flow of a mixture of monoethylene glycol and water. The temperature of the reservoir of the thermostat can be adjusted between −30 and 90 °C. The thermostat is equipped with a proportional-integral temperature controller. Pt100 resistors mounted close to the top (set-up B) or bottom (set-up A) surface holders are used as external sensors for the temperature control. With this configuration, the temperature stability inside the box is better than 10 mK for hours. The thermal response times for the two set-ups differ significantly. For a 1 °C temperature step, the new temperature of set-up B is stabilized within approximately 20 min. Set-up B is thus ideally suited for quick temperature changes. In contrast, set-up A has a much longer thermal response time due to the large heat capacity of the chamber walls. Temperature steps of 1 °C require 2–3 h of equilibration.

2.2. The optical set-up

As already mentioned in the introduction, the measurement of the thickness of confined liquid films relies on multiple-beam interferometry. In contrast to SFA experiments using the conventional fringes of equal chromatic order (FECO) technique, monochromatic light is used here to illuminate the sample. It is generated by passing the light from the Xe arc lamp through a 1/8 m grating monochromator (LOT Oriel, model 77200). The intensity and bandwidth of the transmitted light can be adapted by choosing entrance and exit slits between 0.05 and 3.16 mm. For a typical exit slit width of 0.6 mm in combination with a grating of 1200 l mm^{-1}, the transmitted light has a triangle-shaped intensity distribution around the central wavelength λ_0 with a bandwidth of $\Delta\lambda = 2$ nm, according to manufacturer specifications. A spectral calibration lamp (mercury–argon) with lines at $\lambda_1 = 435.833$ nm and $\lambda_2 = 546.074$ nm is used to calibrate the monochromator. Transmitted light is collected with long distance microscope objectives (Nikon; 5× with NA = 0.13; WD 22.5 mm or 20× with NA = 0.35; WD 20.5 mm) and recorded with a digital CCD camera (PixelFly; PCO computer optics; 1360 × 1024 pixels; 12 bit resolution). The combined lateral resolution is 0.98 and 4.17 pixel μm^{-1} for 5× and for 20× magnification, respectively. The maximum frame rate of the camera is 10 full frames per second. A frame rate of 20 frames per second can be achieved by operating the camera in the 2 × 2 binning mode.

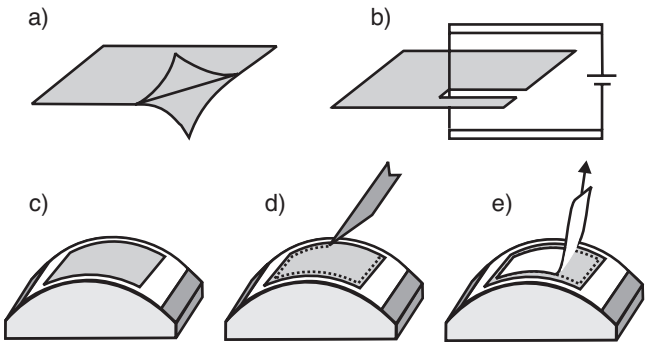

Figure 4. Sample preparation. (a) A large mica sheet is cleaved down to a thickness of approximately 10 μm using a needle. (b) The thin mica sheet is cut into pieces of 1×2 cm^2 with a glowing platinum wire. (c) The mica sheets are glued onto the sample holder with the Ag layer facing the glue. (d) Scratches along the edge of the mica sheet are made with a sharp scalpel to facilitate the subsequent recleavage step. (e) Recleavage of the mica sheet using adhesive tape.

3. Experimental procedures

3.1. Substrate preparation

Reliable SFA experiments with liquid films of a thickness in the nanometre range require substrate surfaces that are atomically smooth over the entire contact area (up to 100 μm in diameter). Mica is the only material which can be prepared with such a high surface quality. The conventional mica sample preparation procedure consists of several successive cleavage steps, until sheets a few micrometres thick and several square centimetres in area are obtained. Subsequently, the thin mica pieces are cut into pieces of approximately (1×2) cm^2 using a glowing platinum wire. Finally, the pieces are deposited onto a freshly cleaved thick mica sheet (backing sheet), which serves as a holder for the subsequent thermal evaporation of the silver mirrors. All these procedure are usually performed inside a laminar flow box. After depositing the silver layers, the mica sheets are carefully removed from the backing sheet and glued onto the glass support (cylindrical lenses or microscope cover slips; see above).

Recently, it was observed that one step in this preparation procedure can lead to significant contamination of the surfaces with nanoparticles [10]: small amounts of Pt evaporate from the glowing Pt wire while the mica sheets are cut. Since the presence of nanoparticles on the surfaces affects the results of SFA measurements [6, 11–14] and may lead to erroneous interpretations, various groups suggested procedures for reducing or eliminating the concentration of contaminants [12, 15, 16]. The method used in our group is based on a procedure first proposed by Frantz and Salmeron [15]: after the mica sheets have been glued to their supports, they are cleaved once more using adhesive tape immediately prior to the experiments (figure 4). This recleavage step guarantees that the surfaces are free of any possible contamination that may have been deposited during any of the preceding preparation steps. Atomic force microscopy images recorded prior to and after recleavage show that nanoparticles initially present on the surfaces are completely removed (figure 5). Furthermore, this procedure has the advantage of removing molecules adsorbed from the atmosphere during the various preparation and handling procedures (including adherence to the backing sheet)[2].

[2] In fact, this was the original motivation of Frantz and Salmeron; see [16]. These authors showed that the adhesion of freshly cleaved dry mica is substantially higher than that of ordinarily prepared mica surfaces, which indicates indeed a reduced coverage with organic contaminants.

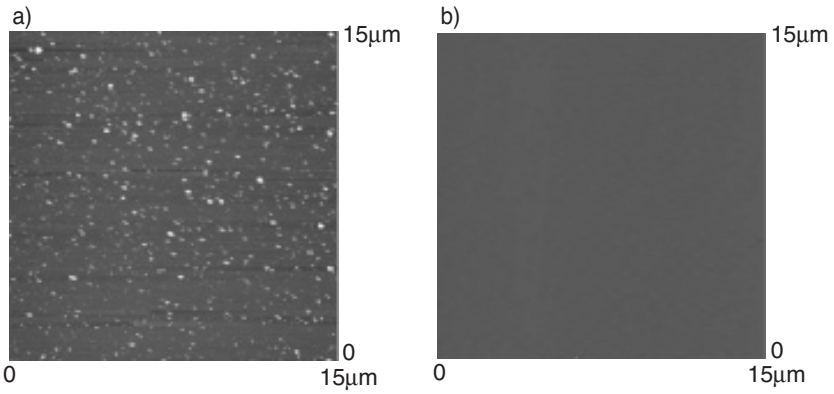

Figure 5. Atomic force microscopy images before (a) and after (b) recleavage. Scan size: $15 \times 15\ \mu m^2$. Typical particle dimensions in (a) are: a few nanometres in height and a few tens of nanometres in diameter.

Two prices have to be paid for this gain in surface cleanliness: first, recleaving can create additional cleavage steps on the surfaces to the extent that the samples become unusable—this problem can be reduced by scratching the mica sheets with a sharp scalpel around the edge before attaching the adhesive tape, as sketched in figure 4(d); second, recleaving reduces the thickness of both mica substrates by some random amount. Therefore, the thicknesses of the two mica sheets are in general different. This asymmetry of mica sheets can be determined in two ways: first, it can be treated as an additional fitting parameter in the numerical analysis of the interferometry data (see below). Second, it can be measured independently by evaporating a second Ag layer onto both mica sheets after the experiment. Being silvered on both sides, each mica sheet acts as a Fabry–Perot interferometer. Hence, the thickness is easily determined by measuring transmission spectra for the individual sheets.

3.2. Sample characterization

At the beginning of each experiment, reference transmission spectra are recorded with the mica surfaces in contact in a dry nitrogen atmosphere[3]. The incident wavelength λ is scanned from approximately 400 to 600 nm using the motorized monochromator. At each wavelength a video image of the transmitted light is recorded; each one shows a series of concentric Newton fringes. The wavelength is scanned in steps between 0.05 and 0.5 nm, depending on the desired spectral resolution. The data acquisition rate is approximately one image per second. A full data set thus contains the transmitted intensity as a function of two spatial coordinates and one spectral coordinate that represents the optical thickness of the sample. In order to analyse the data, we consider various cross sections through this three-dimensional data set. The thickness of the mica sheets in dry contact is determined from one-dimensional cross sections along the spectral direction of the data set, i.e. by plotting the transmitted intensity (at a certain point within the contact area) as a function of wavelength. In order to reduce noise, the intensity is usually averaged laterally over an area of $\approx 5 \times 5\ \mu m^2$ (inside the contact area). A typical spectrum is shown in figure 6. The mica thickness is obtained by optimizing the overlap between the experimental data (data points) and the numerically calculated transmission (solid

[3] For some batches of mica, the adhesion in dry nitrogen is so strong that pulling the surfaces apart again destroys the surfaces. In this case, the 'dry' contact measurements were performed in ordinary laboratory atmosphere, i.e. with a relative humidity of 30–60%, depending on the external conditions.

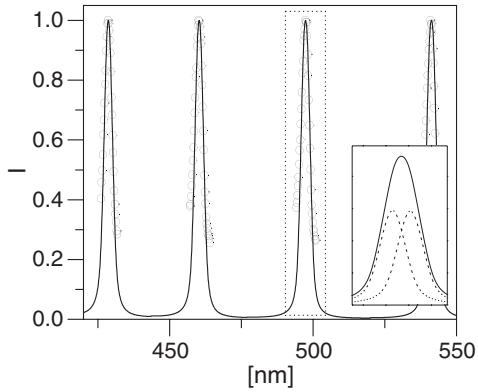

Figure 6. The experimental transmission spectrum (open circles) of two mica surfaces in dry contact. Solid curve: the numerically calculated spectrum (sum of β and γ polarization) for $d_{\text{mica}} = 1.8153$ μm, as obtained from the FSC procedure (see the text for details). Refractive indices for mica of $n_\beta = 1.5794 + 4.76 \times 10^3/\lambda^2$ and $n_\gamma = 1.5546 + 4.76 \times 10^3/\lambda^2$ (λ in nm) for β and γ polarization, respectively, were used. Inset: the transmission calculated for the β and the γ polarization for the dashed box in the main panel. Peak separation: 1.5 nm.

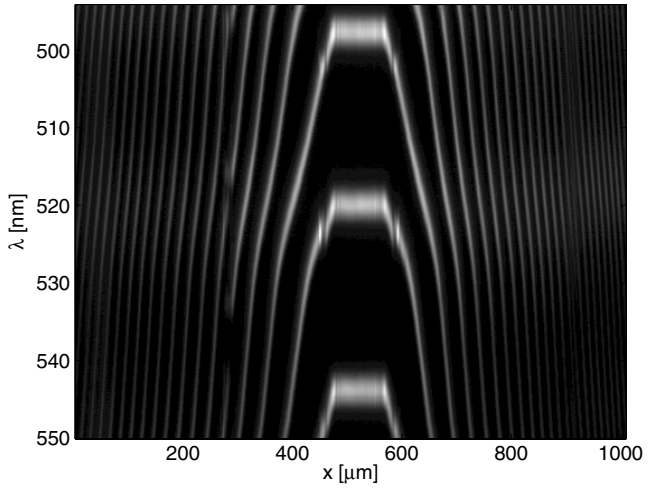

Figure 7. A two-dimensional representation of the interferometry data set along the spectral and one spatial coordinate mimicking conventional FECO data. The break in the fringes just outside the contact area is due to a capillary neck of OMCTS. The spacing between adjacent scans along the spectral dimension is 0.1 nm.

curve) using the fast spectral correlation method (see the next section). Two-dimensional cross sections through the full data sets with the spectral and one spatial dimension are identical to conventional FECO data, as shown in figure 7.

After recording reference spectra in a dry atmosphere, liquid is added to the sample chamber. Small quantities ($\approx$10 μl) of non-volatile liquids are injected with a syringe directly onto the mica surfaces. Volatile wetting liquids (e.g. octamethylcyclotetrasiloxane; OMCTS) are usually injected into a separate container inside the chamber with the mica surfaces in contact. From there, they are transported to the sample via the vapour phase. Capillary condensation in the gap between the two mica surfaces in contact leads to the formation of a

liquid neck (see figure 7) around the contact area within a few tens of minutes, depending on the vapour pressure. This procedure is particularly non-invasive and prevents possible mica flakes produced in the recleavage step from flowing into the contact area. For OMCTS at room temperature, the diameter of the capillary neck reaches about 0.5 mm after approximately one hour.

3.3. Numerical data analysis

The optical transmission through the sample depends on the thicknesses and the refractive indices of the Ag layers, of the mica sheets, and of the liquid layer under investigation (see figure 1(b)). Various methods are available for calculating the transmission spectrum of such a multilayer interferometer. For specific cases, analytical formulae are available. The most general method, however, is the matrix method, which allows calculation of transmission or reflection coefficients for systems with an arbitrary number of parallel layers [17]: it follows from Maxwell's equations that the electric and the magnetic fields at the two surfaces of a dielectric layer, through which a plane electromagnetic wave of wavelength λ is transmitted, are related by a 2×2 matrix $\mathcal{M}(n, d)$ that depends only on the refractive index, the thickness of the layer, and on the angle of incidence. The latter, however, is always 90° in our case. Note that $\mathcal{M}(n, d)$ is complex if the material absorbs light (e.g. the Ag layers). When the plane wave is transmitted through several parallel layers, the electric and magnetic field at the entrance of the first layer and at the exit of the last layer are related by the characteristic matrix $\mathcal{M}_{\mathrm{tot}}$ of the whole stack of layers, which is simply given by the product of the matrices of the individual layers. For our geometry, it is given by

$$\mathcal{M}_{\mathrm{tot}} = \mathcal{M}_{\mathrm{Ag},1} \cdot \mathcal{M}_{\mathrm{mica},1} \cdot \mathcal{M}_{\mathrm{liquid}} \cdot \mathcal{M}_{\mathrm{mica},2} \cdot \mathcal{M}_{\mathrm{Ag},2}. \tag{1}$$

The subscripts indicate the silver, mica, and liquid layers. The transmission coefficient $T(\lambda)$ is given by the ratio of the transmitted and the incident intensity, as usual.

This version of the matrix method does not treat polarization explicitly. This may seem inadequate in view of the birefringence of mica. However, as long as the optical axes of the two mica sheets are aligned and the liquid is isotropic the incoming unpolarized light splits up into two parts, linearly polarized along the two optical axes of mica. These two beams propagate independently and recombine at the exit of the interferometer. Transmission spectra for unpolarized light—as typically used in the experiments—are thus obtained by calculating the transmission coefficients for β and γ polarization independently and by summing the results, i.e. $T(\lambda) = T_\beta(\lambda) + T_\gamma(\lambda)$.

The actual measured transmitted intensity $I_{\mathrm{T}}(\lambda_0)$ at a given wavelength setting λ_0 of the monochromator is obtained by convoluting the numerically calculated $T(\lambda)$ with the triangle-shaped distribution of the incident intensity $I(\lambda)$ around λ_0:

$$I_{\mathrm{T}}(\lambda_0) = \int_{\lambda_0-\Delta\lambda}^{\lambda_0+\Delta\lambda} I(\lambda) T(\lambda)\, \mathrm{d}\lambda. \tag{2}$$

For the typical experimental choice of $\Delta\lambda = 2$ nm (see above), this convolution smears out the two distinct peaks for β and γ polarization and leads to a single broadened transmission peak (see the inset of figure 6). Only for the narrowest wavelength distribution (which requires rather long CCD exposure times) can the two peaks be resolved individually.

The function $I_{\mathrm{T}}(\lambda_0)$ as given by equation (2) depends on the (wavelength-dependent) refractive indices and thicknesses of all the five layers in the system, whereas the thickness (and sometimes the refractive index) of the liquid layer is the only quantity of interest. In order to analyse the experimental data we need to determine independently as many of these parameters as possible. First, the thickness of the Ag layers is known from the preparation

process. Experimentally, one typically chooses $d_{\mathrm{Ag}} \approx 50$ nm. For thinner films, the reflectivity is not yet at its maximum; for thicker ones, absorption reduces the transmission. For the calculations, d_{Ag} is not a very crucial parameter. Variations of a few nanometres affect the transmitted intensity. Shifts of the peak positions, however, are negligible. The Ag dispersion relation is taken from the literature [18].

The further data analysis is based on the optimization of the overlap between the experimentally determined transmission spectra and the calculated spectra. In principle, this can be done using least squares fitting. However, such a procedure would be rather time-consuming. Instead, we adopted the fast spectral correlation (FSC) procedure suggested by Heuberger [19]. The principle of FSC is the following: instead of computing the entire transmission spectrum for each trial value of d_{mica}, I_{T} is only calculated for those wavelengths λ_i at which transmission peaks were found experimentally. For N peaks, the quantity

$$\Omega = \sum_{i=1}^{N} I_{\mathrm{T}}(\lambda_i) \tag{3}$$

is calculated and maximized as a function of the thickness and/or refractive index of the remaining layers. In principle, the number of parameters that can be determined is the same as the number of peaks that were measured. In practice, however, it turns out that there are many local maxima of Ω with rather similar absolute values if several unknown parameters are to be determined simultaneously. Therefore, the properties of the mica layers are determined from the reference measurements described above. The dry contact spectrum shown in figure 6 was analysed as follows: the mica dispersion relation was adopted from the literature [20]. The mica thickness is the sum of those of the two mica sheets: $d_{\mathrm{mica}} = d_{\mathrm{mica},1} + d_{\mathrm{mica},2}$, and $d_{\mathrm{liquid}} = 0$. The solid curve in figure 6 shows the full transmission spectrum calculated for the optimum value of d_{mica} obtained by maximizing Ω, as just described. For this specific data set, we found $d_{\mathrm{mica}} = 1.8153\ \mu$m. Deviations between the calculated and the experimentally determined peak positions are usually less than 0.1 nm. As mentioned above, both mica sheets were coated with a second Ag layer after the experiment, such that $d_{\mathrm{mica},1}$ and $d_{\mathrm{mica},2}$ could be determined independently. In this specific experiment, we found $d_{\mathrm{mica},1} = 1.2184\ \mu$m and $d_{\mathrm{mica},2} = 0.5972\ \mu$m. The sum agrees with the result of the reference measurement to within 0.3 nm.

4. High speed two-dimensional imaging

The acquisition of the full three-dimensional interferometry data set described so far is rather slow. If the wavelength is fixed, however, two-dimensional images can be acquired at the video rate. In order to preserve the high resolution as regards the film thickness, the incident wavelength is adjusted to the wing of one of the transmission peaks in the reference spectrum (figure 6). Under these conditions, variations in the film thickness of less 0.1 nm lead to significant changes in the transmitted intensity. In figure 8(a), we show the transmitted intensity inside the contact area as a function of time as the two surfaces are pressed together at a loading rate of 1.9 mN s^{-1}. In this case, λ_0 was fixed to 499 nm, i.e. on the long wavelength wing of the peak close to 500 nm in figure 6. While the intensity varied continuously at large surface separation ($t < 2$ s), a series of discrete steps appeared as the surfaces came closer. As we will show below, each step corresponds to a reduction in film thickness by one molecular layer. There are two methods for quantifying the thickness change. First, we can calculate $I_{\mathrm{T}}(\lambda_0)$ as a function of d_{liquid} using the thickness of the two mica sheets, as determined above. Second, we can stop the load ramp at various loads corresponding to the plateaus in figure 8(a) and scan λ_0 in narrow ranges in order to determine the positions of the transmission peaks with high

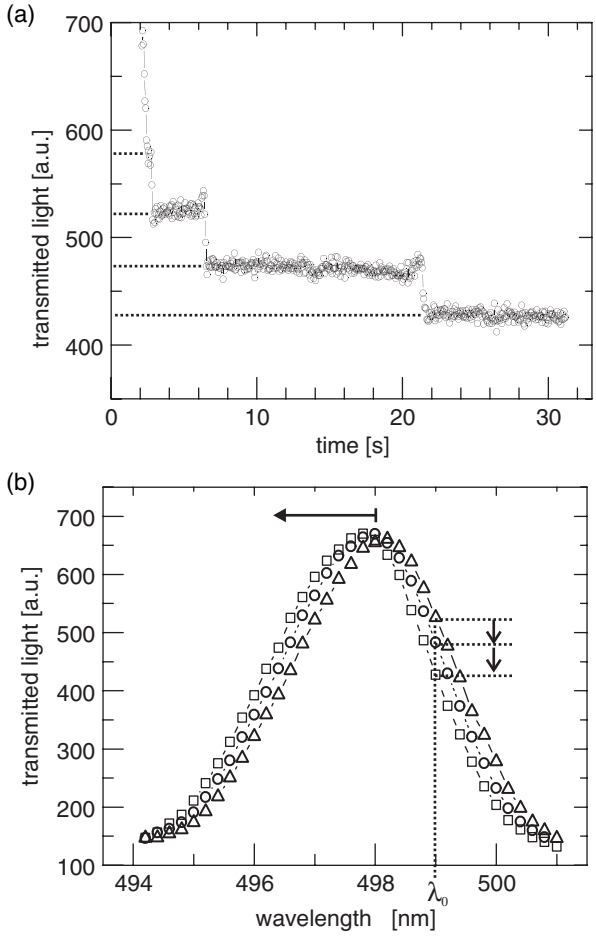

Figure 8. (a) Transmitted intensity within the contact area versus time. Arrows indicate the intensity levels at which the spectra in panel (b) were measured (lateral averaging range: $5 \times 5\ \mu m^2$; $\lambda_0 = 499.0$ nm; loading rate: $1.92\ mN\,s^{-1}$). (b) The position of the transmission peak corresponding to the arrows in panel (a). Triangles: first plateau; circles: second plateau; squares: last plateau.

accuracy. Figure 8(b) shows that the position of one of the peaks does indeed shift to smaller wavelengths as the intensity between consecutive plateaus decreases, i.e. the film thickness decreases as well. Assuming a constant bulk refractive index of OMCTS, an FSC analysis of the data shows that the thickness of the liquid film was 2.78, 2.01, and 1.49 nm for the three peaks from right to left, respectively. The decrease per step is thus slightly less than is usually found in conventional FECO measurements with the same system [5–8]. However, it should be noted that the data were acquired at a normal pressure of ≈20 MPa, which is substantially higher than in other experiments.

The key advantage of the imaging technique is that dynamic processes can be imaged in real time. In figure 9, we show a series of video snapshots recorded during the transition from the second last to the last plateau in figure 8(a) (around $t = 20$ s). The first image shows a homogeneous intensity within the contact area corresponding to a homogeneous film thickness. In the second image, a small area appears close to the centre of the contact area where the film

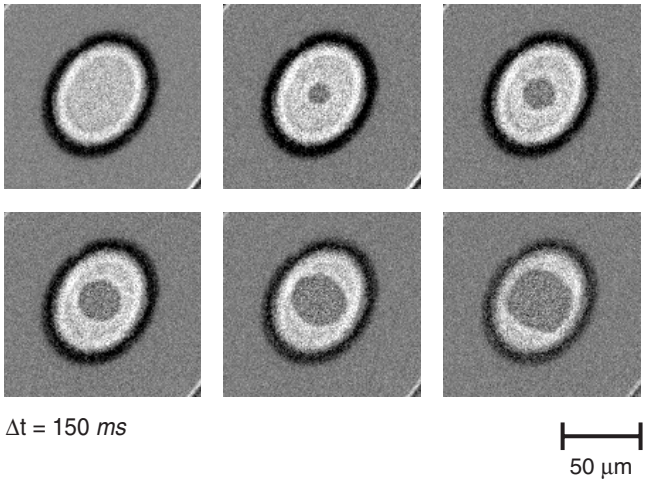

Figure 9. A video sequence of a squeeze-out event for OMCTS corresponding to the last transition in figure 8(a) ($\lambda_0 = 499.0$ nm; loading rate: 1.92 mN s^{-1}).

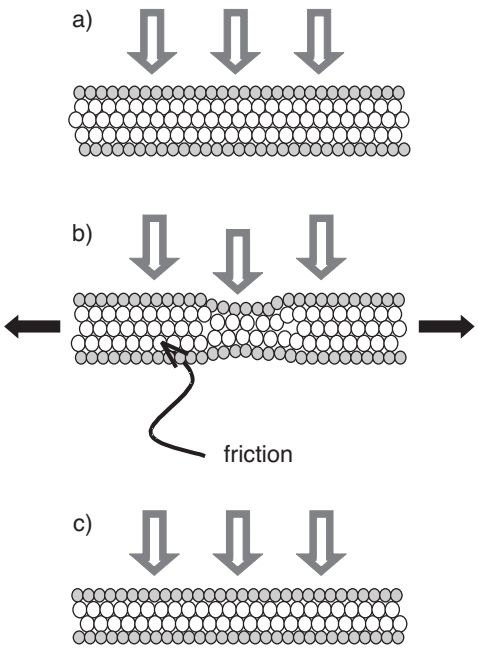

Figure 10. A schematic diagram of a layer squeeze-out event. Grey: substrate atoms; white: liquid molecules. Vertical arrows indicate the applied normal pressure. (a) The initial state with constant film thickness; (b) an intermediate state with locally reduced thickness and a moving boundary line; arrows indicate the direction flow during squeeze-out; (c) the final state (constant thickness).

thickness is locally reduced by one molecular layer. Within a few hundred milliseconds, this area spreads across the whole contact area until the thickness is homogeneous again. Figure 10 illustrates the microscopic processes involved in the collapse of the lubricant layer, as first suggested by Persson and Tosatti [21]. The initial state with a thickness of n layers becomes unstable due to the increasing normal pressure. When a sufficiently large density fluctuation

appears within the liquid film, the mica substrates relax elastically and stabilize this region of reduced film thickness. The nucleus begins to grow if the gain in elastic energy exceeds the energetic penalty due to line energies along the edge of the nucleus. The critical radius for the nucleation cannot be observed experimentally. It is estimated to be of the order of 1 nm [21]. Elastic relaxation of the substrates is also the driving force for the growth that is observed experimentally (see figure 10). During the growth phase, the elastic driving force is balanced by any kind of dissipation occurring during the squeeze-out process. Phenomenologically, the dissipation can be characterized by an effective viscosity [21]. It turned out that this simple model is very successful in describing the motion of the boundary line of the growing nucleus. A variety of aspects have been studied over the past few years: the area of the growing nucleus as a function of time is well reproduced [22]. If the nucleation of the reduced film thickness takes place in the centre of the contact area, the dynamics of the roughly circular boundary line can be described analytically. If the nucleation happens far away from the centre of the contact area, the boundary line assumes a characteristic double S-shape [23]. In this case, a quantitative description can only be obtained numerically [22]. If the mica sheets are particularly thin, the boundary line may become unstable and roughen during the growth phase [24]. This can even lead to the formation of trapped pockets of liquid left behind in the contact area in the final stage of the collapse. When particularly thin mica sheets are approached at high rates, elastohydrodynamic deformation of these soft substrates leads to simultaneous nucleation of the layer collapse at several positions along the rim of the contact area [25]. An overview of these processes was given in a recent review article by Persson and Mugele [26]. Finally, it was possible to determine the thickness dependence of the effective viscosity of molecularly thin lubricant layers [27]. For a specific model lubricant, it was found that the effective viscosity increases by approximately one order of magnitude upon decreasing the film thickness from six to two layers. This result was remarkable, because it was in contrast to earlier results that reported an increase in the viscosity by several orders of magnitude within roughly the same range of film thickness [6, 7]. In the meantime, some of these earlier results, which were all based on force measurements, were traced to surface contamination by nanoparticles [14]. Careful and clean surface preparation such as that described in this paper is thus of crucial importance. It is also worth noting that the sensitivity of the two-dimensional imaging technique in terms of effective viscosity is about two orders of magnitude better than the highest reported resolution in shear force measurements [7].

5. Summary

We described the experimental set-up and procedures, and new experimental techniques, for studying molecularly thin lubricant layers. Recleavage of mica substrates immediately prior to the experiment was described and shown to be a successful procedure for avoiding surface contamination with nanoparticles. The two-dimensional imaging technique presented here allows unprecedented insights into the stability and the collapse dynamics of liquid films with a discrete layer structure.

Acknowledgments

We thank Stephan Herminghaus for discussions and for the stimulating atmosphere within the Applied Physics Department. Funding was provided by the German Science Foundation (Grant No Mu1472/2) within the priority programme ‘Wetting and Structure Formation at Interfaces’.

References

[1] Persson B P 2000 *Sliding Friction* (*NanoScience and Technology*) 2nd edn, ed R W K von Klitzing (Berlin: Springer)
[2] Israelachvili J N 1992 *Intermolecular and Surface Forces* 2nd edn (London: Academic)
[3] Horn R G and Israelachvili J N 1981 *J. Chem. Phys.* **75** 1400
[4] Israelachvili J N, McGuiggan P M and Homola A M 1988 *Science* **240** 189
[5] Christenson H K and Blom C E 1987 *J. Chem. Phys.* **86** 419
[6] Demirel A L and Granick S 1996 *Phys. Rev. Lett.* **77** 2261
[7] Klein J and Kumacheva E 1995 *Science* **269** 816
[8] Klein J and Kumacheva E 1998 *J. Chem. Phys.* **108** 6996
[9] Mugele F, Becker T, Klingner A and Salmeron M 2002 *Colloids Surf.* A **206** 105
[10] Ohnishi S, Hato M, Zamada K and Christenson H K 1999 *Langmuir* **15** 3312
[11] Heuberger M, Zäch M and Spencer N D 2001 *Science* **292** 905
[12] Heuberger M and Zäch M 2003 *Langmuir* **19** 1943
[13] Lin Z and Granick S 2003 *Langmuir* **19** 7061
[14] Zhu Y and Granick S 2003 *Langmuir* **19** 8148
[15] Frantz P and Salmeron M 1998 *Tribol. Lett.* **5** 151
[16] Israelachvili J N, Alcantar N A, Maeda N, Mates T E and Ruths M 2004 *Langmuir* **20** 3616
[17] Born M and Wolf E 1999 *Principles of Optics* 6th edn (Cambridge: Cambridge University Press)
[18] Johnson P B and Christy R W 1972 *Phys. Rev.* B **6** 4370
[19] Heuberger M 2001 *Rev. Sci. Instrum.* **72** 1700
[20] Mangipudi V S 1995 *J. Colloid Interface Sci.* **175** 484
[21] Persson B N J and Tosatti E 1994 *Phys. Rev.* B **50** 5590
[22] Zilberman S, Becker T, Mugele F, Persson B N J and Nitzan A 2003 *J. Chem. Phys.* **118** 11160
[23] Mugele F and Salmeron M 2000 *Phys. Rev. Lett.* **84** 5796
[24] Zilberman S, Persson B N J, Nitzan A, Mugele F and Salmeron M 2001 *Phys. Rev.* E **63** 055103
[25] Becker T and Mugele F 2003 *J. Phys.: Condens. Matter* **15** S321
[26] Persson B and Mugele F 2004 *J. Phys.: Condens. Matter* **16** R1
[27] Becker T and Mugele F 2003 *Phys. Rev. Lett.* **91** 166104